THE JOURNAL OF PHYSICAL CHEMISTRY A

Article

pubs.acs.org/JPCA

Ion Mobility Spectrometry, Infrared Dissociation Spectroscopy, and ab Initio Computations toward Structural Characterization of the Deprotonated Leucine-Enkephalin Peptide Anion in the Gas Phase

Florian Schinle,[†] Christoph R. Jacob,*[,‡,∥] Arron B. Wolk,[§] Jean-François Greisch,[†] Matthias Vonderach,[∥] Patrick Weis,[∥] Oliver Hampe,[†,∥,#] Mark A. Johnson,*[,§] and Manfred M. Kappes*[,†,‡,∥]

[†]Institute of Nanotechnology, Karlsruhe Institute of Technology (KIT), 76021 Karlsruhe, Germany

[‡]Center for Functional Nanostructures, Karlsruhe Institute of Technology (KIT), Wolfgang-Gaede-Strasse 1a, 76131 Karlsruhe, Germany

[§]Sterling Chemistry Laboratory, Yale University, P.O. Box 208107, New Haven, Connecticut 06520, United States

[∥]Institute of Physical Chemistry, Karlsruhe Institute of Technology (KIT), 76128 Karlsruhe, Germany

Supporting Information

ABSTRACT: Although the sequencing of protonated proteins and peptides with tandem mass spectrometry has blossomed into a powerful means of characterizing the proteome, much less effort has been directed at their deprotonated analogues, which can offer complementary sequence information. We present a unified approach to characterize the structure and intermolecular interactions present in the gas-phase pentapeptide leucine-enkephalin anion by several vibrational spectroscopy schemes as well as by ion-mobility spectrometry, all of which are analyzed with the help of quantum-chemical computations. The picture emerging from this study is that deprotonation takes place at the C terminus. In this configuration, the excess charge is stabilized by strong intramolecular hydrogen bonds to two backbone amide groups and thus provides a detailed picture of a potentially common charge accommodation motif in peptide anions.

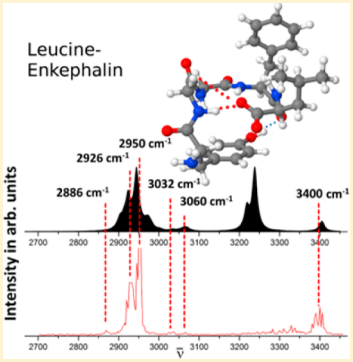

INTRODUCTION

Understanding and predicting the structural behavior of biomolecules (e.g., aggregation of peptides[1]) from first-principles is one of the grand challenges for contemporary physical chemistry. Our ability to obtain three-dimensional structures of (bio)molecular gas-phase ions has made great strides over the past few years as a result of dramatic improvements in shape analysis by ion-mobility[2−7] and bond-specific contact determination of compact structure with mass-selective vibrational spectroscopy.[8−13] In particular, recently developed cryogenic processing of mass-selected ions stored in low-temperature ion traps[14−18] has helped in many cases to overcome spectral congestion by reducing the conformational phase space accessible at elevated temperatures.

The focus of the mass spectrometry based characterization of peptides, including the prevalent field of proteomics,[19] has been on cations, whereas research on structure and fragmentation mechanisms of anionic peptides is still in its infancy. With recent instrumental developments in fast polarity switching,[20] it is now possible to collect both cation and anion mode MSMS spectra of peptide digests without degrading the quality of the cation fragmentation data, opening up the prospect of increasing peptide sequence coverage with complementary anion fragmentation data. Collision-induced dissociation tandem mass spectrometry on deprotonated peptides has been shown to mostly yield b- and y-type fragments as well as c-ions with a strong side chain dependence.[21−24] As in the cations' case, it is important to characterize the basic charge accommodation motifs in the anionic analogues to provide a rationale for their observed fragmentation patterns.

In this study, we explore the preferred gas-phase structures of the pentapeptide leucine-enkaphaline anion. The investigation of anionic species can prove especially difficult as illustrated by the recent literature on cysteine, where infrared and photoelectron studies are in disagreement about the deprotonation site,[25,26] and in fact the answer may depend on electrospray conditions/solvents used to form the gas-phase anion.[27,28] In this study we explore the preferred gas-phase structures of this prototypical peptide by using infrared multiple photon dissociation (IRMPD) spectroscopy, cryogenic ion vibrational predissociation (CIVP) spectroscopy, and ion-mobility spectrometry, which are complemented by quantum-chemical calculations based on density-functional theory. We analyze the characteristic vibrational signatures of intramolecular hydrogen bonding through a comparison of the single- and

Special Issue: A. W. Castleman, Jr. Festschrift

Received: February 19, 2014
Revised: May 31, 2014
Published: June 2, 2014

   dx.doi.org/10.1021/jp501772d | J. Phys. Chem. A 2014, 118, 8453−8463

multiple-photon mass selected infrared spectra. The aim of this endeavor is to pair the complementary structural information obtained from mass selective infrared spectroscopy and ion mobility spectrometry with standard collision-induced dissociation spectrometry to characterize the internal solvation of deprotonated carboxylate groups.

Leucine-enkephalin is a pentapeptide with YGGFL primary sequence (Scheme 1) and has been mostly studied in the gas

Scheme 1. Lewis Structure of Neutral Leucine-Enkephalin with Numbering of the Position of Possible H-Bond Donors (Hydrogen Atom) and Acceptors (Oxygen Atom of Amide Group) As Used Throughout the Text

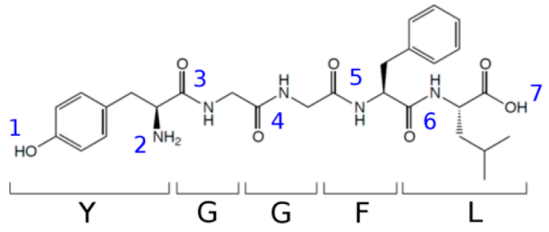

phase as a protonated species,[29] including IR spectroscopic indications that a mobile proton is at play under ambient temperatures conditions.[30] The structures of some of its major fragments remain of fundamental interest, with macrocyclic structures for the a_4 fragment being found recently by elegant IR-UV double resonance spectroscopy at cryogenic temperatures.[31] Under the same experimental conditions, such a ring formation was excluded for the b-ions of YGGFL,[31] though cyclic isomers had been observed previously at room temperature.[32] With the large body of work on its protonated analogue, the YGGFL anion offers an ideal system to further a basic understanding of the effects of deprotonation on gas-phase peptide structure.

EXPERIMENTAL AND COMPUTATIONAL METHODS

A. Mass Spectrometry. All experiments described were performed on electrosprayed gas-phase anions of leucine-enkephalin. In general, a solution of commercially available leucine-enkephalin acetate salt hydrate (cat# L9133, Sigma-Aldrich) was prepared as a stock solution in pure water at a typical concentration of 10^{-5} mol/L. It was found that adding 5% (vol) of a 5 M ammonium acetate solution (cat# 09691, Sigma-Aldrich) improved ion intensity and stability. The low temperature IRPD measurements were performed with a mixture of this stock solution with methanol (1:4 v%/v%).

A.1. Collision-Induced Dissociation (CID) Mass Spectrometry. Collision-induced dissociation (CID) was performed on a LTQ-Orbitrap XL ETD mass spectrometer (ThermoFisher Scientific, San Jose, CA, USA). The solutions used were prepared as described above. The ions were generated with electrospray ionization and spraying conditions were optimized with respect to the intensity of the parent anion (m/z 554.26) at the detector of the linear ion trap. For LTQ-Orbitrap measurements the following protocol was used: precursor ion (MS1) isolation at m/z 554.26 with a mass selection window of 3.0 amu, for CID with helium resonant radio frequency excitation at m/z 554.26 was applied. The collision energy was tuned stepwise between 0 and 30 in steps of 1 (in internal units), and the corresponding fragment ions were recorded in the Orbitrap mass analyzer over a mass range of 150−700 m/z. Analysis of the mass spectra was aided by the XCalibur Software package (vs 2.1, Thermo Fisher Scientific).

A.2. Ion Mobility Spectrometry (IMS). Experiments were performed on a home-built instrument that couples IMS with photoelectron spectroscopy described in detail elsewhere.[5,33] Briefly, an electrospray ionization source is interfaced to a dc mobility drift cell by an hourglass shaped ion funnel. The room temperature drift cell is operated at a helium pressure of about 2.5−3 mbar and at a homogeneous drift field of 10 V/cm. The injection energy of the ions, i.e., the difference between the dc voltages of the funnel exit electrode and the entrance electrode of the drift cell, can be varied over a range of 10−100 V. Ions leaving the drift cell are detected after being discriminated according to their mass-to-charge ratio by means of a quadrupole mass filter to yield arrival time distributions. From the arrival time distribution the reduced ion mobility (zero field limit)[34] and the collision cross sections (ccs) are derived.

B. Vibrational Spectroscopy. *B.1. Infrared Multiphoton Dissociation (IRMPD) Spectroscopy.* Infrared multiple photon dissociation (IRMPD-) spectroscopy was performed in a 7T-FT-ICR mass spectrometer (Bruker Daltonics, Billerica, MA, USA). The mass spectrometric setup[35,36] as well as the laser spectroscopic method have been described in detail previously.[37] Electrosprayed ions are fed into a desolvation capillary (with 0.5 mm inner diameter) held at ∼100 °C. A home-built ion funnel was used to focus the ions, while reducing the amount of neutral molecules by using a jet disrupter.[38] The ions were stored in a home-built hexapole trap for typically 0.8 s before being pulsed into the ICR cell (Bruker's Infinity cell). The hexapole was modified to feature additional molybdenum wires, which are attached between the rods in a tapered fashion so as to create an axial dc potential gradient, similar to the proposal by Marshall et al.[39] Ions were then trapped on the fly by pulsing the trapping voltages of the ICR cell open for an appropriate time, here ∼1.0 ms.

The cell itself is enclosed in a copper jacket that was either held at room temperature or cooled to ∼160 K by a controlled flow of liquid nitrogen. The detailed design of the modified ICR cell is described elsewhere.[40,41] For experiments with a cooled trap, a 1.0 s delay after storage of the ions was implemented to allow the ions time to thermalize by radiative cooling. The ions of interest were mass-selected in the ICR cell by an isolation pulse before being irradiated with laser light.

Infrared light was generated with a Nd:YAG-pumped OPO/OPA parametric oscillator (LaserVision, Bellevue, WA, USA). The laser beam is focused into the ICR cell by a CaF_2 lens with 750 mm focal length entering the ultrahigh vacuum chamber through a CaF_2 zero length viewport (MDC Vacuum Ltd., East Sussex, U.K.) mounted onto the cell flange. The laser power was monitored by sending a reflection from a CaF_2 wedge onto a pyroelectric detector (Coherent, 33-1140 and read out unit Field Master GS). The number of laser pulses allowed into the ion cell was controlled by a TTL-pulse-driven electromechanical shutter (Newport, Model 845 HP).

An in-house written software suite was used to record the data. The laser was scanned through the IR range with discrete step sizes of 2 cm^{-1}. At each step, mass spectra with and without laser irradiation were recorded along with the laser power. Scans were taken by recording a preset number of mass spectra (typically 4). To obtain photofragment mass spectra, the trapped ions were irradiated for 2 s corresponding to 40

dx.doi.org/10.1021/jp501772d | J. Phys. Chem. A 2014, 118, 8453−8463

laser pulses (at a repetition rate of 20 Hz) with each laser pulse being 6−8 ns long. Infrared action spectra were evaluated from the mass spectra by taking the difference between intensities of laser-induced fragment ions and fragment ion intensities without laser from the reference mass spectra (i.e., baseline correction). This difference was normalized to parent ion intensity of the reference spectra, or equivalently, to the sum of parent and fragment ion intensities with the laser on (eq 1). No explicit correction for relative laser output was taken into account, though relative laser power was recorded in each scan to ensure a smooth laser power curve avoiding any spectral artifacts due to laser fluctuations.

$$\frac{I}{I_0} = \frac{\sum I_{\text{frag}}}{I_{\text{parent}} + \sum I_{\text{frag}}} \quad (1)$$

B.2. Infrared Predissociation Spectroscopy. The Yale Photofragmentation Spectrometer has been described in detail elsewhere.[42] Briefly, electrosprayed ions were guided through a skimmer and two apertures to a final pressure of 2×10^{-7} Torr using radio-frequency-only quadrupoles and octopoles. After turning 90° in a dc-only quadrupole, the ions were guided in a quadrupole ion trap (QIT, Jordan TOF) mounted to a closed-cycle helium cryostat (Sumitomo RDK-415E) held at 10 K. He buffer gas (10% D_2 by volume) was injected into the trap by a pulsed valve (Parker series 99) to capture the ions. D_2 adducts of deprotonated leucine-enkephalin were observed tens of milliseconds after the gas pulse and continued to increase in abundance until trap ejection at 95 ms. The ions were then injected into a Wiley−McLaren time-of-flight mass spectrometer where they were intersected with the output from an OPO/OPA parametric oscillator (LaserVision, Bellevue, WA, USA) at the temporal focus. Finally, photoproducts were separated from intact D_2 adducts in a secondary reflectron and detected with microchannel plates.

To ensure the predissociation spectrum is linear in laser fluence, the output of the OPO/OPA was lowered until a linear photofragmentation response was observed for all transitions. For the 800−2300 cm^{-1} range, the signal and idler beams are mixed in a $AgGaSe_2$ crystal, increasing the bandwidth of the laser from ∼3 cm^{-1} in the 2300−4000 cm^{-1} range to ∼6 cm^{-1} after conversion to the lower energy photons. The CIVP signal is reported as the photoproduct yield as a function of excitation laser wavelength normalized to laser pulse energy.

B.3. Computational Details. To generate candidate structures, we started with molecular dynamics (MD) simulations on the leucine-enkephalin anion, including various deprotonation sites, using Xleap in conjunction with the AMBER-99 force-field as part of the AMBER7 package.[43] During these simulations, we used simulated annealing with a maximum temperature of 500 K, a minimum temperature of 300 K, and a MD time of 50 ps to produce approximately 500 structures. Subsequently, a full geometry optimization using the AMBER force field was performed for each of these structures. In a second step, the 500 candidates we optimized using the semiempirical PM6 method with MOPAC.[44] The 50 candidates with the lowest PM6 energy were then sorted according to their structure-type and the refined structures were used as starting point for a full geometry optimization using quantum-chemical calculations performed with the program package TURBOMOLE (version 6.3.1)[45] using density-functional theory. The BP86 exchange−correlation functional[46,47] has been applied in combination with the def2-TZVP basis set of Weigend et al.[48] To improve the description of dispersion interaction, which is missing in generalized-gradient approximation functionals such as BP86, the empirical dispersion correction by Grimme[49,50] (BP86+D3) has been employed in single-point calculations of all geometries and in full geometry optimizations for determining the conformer energies. In addition, single-point MP2 and spin-component scaled (SCS) MP2[51] calculations have been performed. For the calculation of the vibrational infrared spectra, the program package MoViPac[52,53] has been employed. The single-point calculations of energies and gradients for displaced structures, which are needed for the seminumerical calculation of the second derivatives of the molecular electronic energy, have been performed using Turbomole 6.3.1 with BP86/def2-TZVP. As accepted standard in IRMPD spectroscopy, the harmonic values are scaled for comparison with experiment. The use of the free N−H stretch modes as a benchmark results in a scaling factor of 0.987, which is in good agreement with a recently published study on BP86 scaling factors suggesting a value of 0.989 proposed by Wilson and co-workers.[54]

RESULTS AND DISCUSSION

Our discussion of the experimental and computational results is organized as follows: after a mass spectrometric characterization of deprotonated leucine-enkephalin comprising results from MS−MS and ion mobility spectrometry experiments, we present and discuss theoretical predictions of the possible isomeric/conformational structures. Their respective properties, such as collision cross sections and vibrational frequencies, are then compared to experimental data to identify structural candidates consistent with the experimental data.

A. Mass Spectrometric Analysis. *A.1. Collision-Induced Dissociation.* Figure 1 presents the collision-induced dissociation (CID) mass spectrum starting from the isolated deprotonated leucine-enkephalin anion at a nominal excitation amplitude of 22 V. The fragment mass spectrum is dominated by b- and c-type fragments[55,56] with some y-type fragments also being observed with a much smaller intensity.

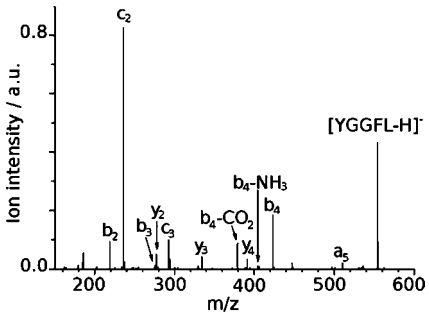

Figure 1. Fragmentation mass spectrum of deprotonated [YGGFL − H]$^-$ obtained after collision-induced dissociation with helium in the linear quadrupole trap of a LTQ Orbitrap instrument. Assignment is based on the mass/charge values as given in Table 1.

This directly suggests that fragments with the negative charge residing on the N-terminus are preferentially formed, as the sparse y-type ions give the charge on the C-terminus. A more detailed representation of the CID experiments is shown in Figure 2, which displays the relative fragment ion distribution as a function of excitation strength applied to the parent anion. At all excitation energies, the major fragment ions are b4 (m/z 423) and c2 (m/z 236). Formation of the b4 ion must involve a

dx.doi.org/10.1021/jp501772d | J. Phys. Chem. A 2014, 118, 8453−8463

Table 1. Experimental and Calculated Monoisotopic *m/z* Values and Assignment of the Fragment Ions of [YGGFL − H]⁻

exp *m/z*	anion stoichiometry	assignment	calc *m/z*	deviation
179.081	$C_9H_{11}O_2N_2$		179.0826	−0.0016
219.076	$C_{11}H_{11}O_3N_2$	b_2	219.0764	−0.0004
236.102	$C_{11}H_{14}O_3N_3$	c_2	236.1029	−0.0009
276.097	$C_{13}H_{14}O_4N_3$	b_3	276.0990	−0.0022
277.153	$C_{15}H_{21}O_3N_2$	y_2/[FL − H]⁻	277.1558	−0.0028
293.123	$C_{13}H_{17}O_4N_4$	c_3	293.1255	−0.0025
294.107	$C_{13}H_{16}O_5N_3$		294.1095	−0.0025
334.174	$C_{17}H_{24}O_4N_3$	y_3/[GFL − H]⁻	334.1772	−0.0022
379.174	$C_{21}H_{23}O_3N_4$	b_4-CO_2	379.1766	−0.0026
391.195	$C_{19}H_{27}O_5N_4$	y_4/[GGFL − H]⁻	391.1987	−0.0037
406.136	$C_{22}H_{20}O_5N_3$	b_4-NH_3	406.1397	−0.0033
423.163	$C_{22}H_{23}O_5N_4$	b_4	423.1662	−0.0032
510.269	$C_{27}H_{36}O_5N_5$	a_5	510.2722	−0.0032
554.257	$C_{28}H_{36}O_7N_5$	[YGGFL − H]⁻	554.2609	−0.0031

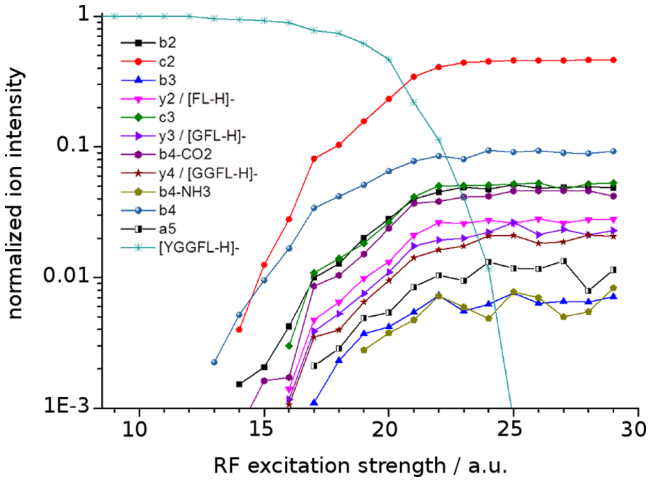

Figure 2. Semilogarithmic plot of normalized fragment ion intensities ("breakdown curve") from low-energy collision-induced dissociation of [YGGFL − H]⁻.

proton transfer step, but from these data we cannot determine whether the intense b4 fragment is directly formed from the parent anion or whether it arises as a secondary fragment from a5, i.e., [YGGFL − H − CO_2]⁻, by way of neutral amine loss. The latter mechanism has been suggested recently for smaller di- and tripeptide anions,[57,58] for which intramolecular stabilization of a C-terminal charge by hydrogen bonds is less likely than in a pentapeptide. It is also worth noting that there is no indication of a sequence scrambling which could follow from the formation of a cyclic b4 structure.

Differences in the fragment intensity are observed among the peaks b4-NH_3 (*m/z* 406), as well as for the b3 and b2 ions with *m/z* 276 and *m/z* 219, respectively, as their relative intensities are strongly increased in the photodissociation spectrum (not shown here). These differences may be attributable to the fact that IR photoexcitation performed with multiple laser pulses may excite fragments as well (depending on their vibrational resonances) whereas in CID experiments it is only the precursor anion that is resonantly energized in the RF trap.

As a more detailed analysis of the dissociation behavior and its mechanistic implications is beyond the scope of this publication, we note here that the major fragment channels appear to be the same as in photofragmentation using infrared laser excitation with minor differences in relative ion intensities.

A.2. Ion Mobility Spectrometry. The arrival time distribution (ATD) measured in the ion mobility experiments of deprotonated leucine-enkephalin [YGGFL − H]⁻ is shown in Figure 3 and consists of a single feature. Fitting this data with

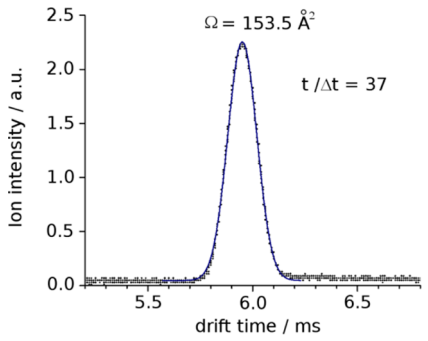

Figure 3. Arrival time distribution (ATD) of leucine-enkephalin anions. The experimental data points are fitted with a single Gaussian function.

one symmetric Gaussian function leads to a center position corresponding to a collision cross section (ccs) of 153.5 Å² and a full-width at half-maximum of 4 Å² (2.7%), which is close to the experimental resolution of the instrument ($t/\Delta t$ = 45).[5]

To the best of our knowledge there is no previous account on the ccs for this peptide anion, but we note in passing that the corresponding value is significantly smaller than the cross sections recently reported for the *protonated* cation [YGGFL + H]⁺ of Ω = 162 Å² by Clemmer et al.[59] and Ω = 165 Å² by Ruotolo et al.,[60] indicating that the anion folds more compactly than its protonated analogue.

B. Computed Structures and Structural Refinement by IMS. With the experimental collision cross section of the LE anion in hand, we carried out a computational search of the conformational landscape to identify classes of locally stable structures. We investigated the two most acidic deprotonation sites: the C-terminal leucine (leading to a carboxylate) and the N-terminal tyrosine (giving rise to a phenolate). In spite of the fact that there could be intermediate tautomeric structures, we started with these limiting anionic structural motifs, which are thereafter called carboxylate and phenolate structures. Within each of these two motifs, we generated about 200 trial structures as described above, which were subsequently geometry optimized using PM6. Of these, the energetically most favorable 16 phenolate and 27 carboxylate structures were subjected to another geometry optimization using both BP86/def2-TZVP and BP86+D3/def2-TZVP. In addition, single-point calculations were performed for the resulting structures using BP86-D3/def2-TZVP, MP2/def2-TZVP, and SCS-MP2/def2-TZVP to verify the relative energies of the conformers. The results are summarized in Table 2 for the lowest-energy isomers, and the results for all considered isomers are given in the Supporting Information.

Visual inspection indicates that one can form subsets of structures based on the major type and position of hydrogen bonds formed to stabilize the negative charge. Within these subsets, in what follows labeled with capital letters (A, B, ...), the conformers mainly differ in the relative orientation of the phenyl and isopropyl side chains of the phenylalanine and the leucine residues, respectively.

dx.doi.org/10.1021/jp501772d | J. Phys. Chem. A 2014, 118, 8453−8463

Table 2. Calculated Energies (eV) of the Most Stable Phenolate and Carboxylate Isomers of Leucine-Enkephaline Considered Initially[a]

	energy					
	BP86			BP86+D3		
geometry	BP86	BP86+D3	MP3	BP86+D3	MP2	SCS-MP2
			Phenolate Structures			
phen-C1	0.2172	0.0219	0.3407	−0.1081	0.2041	0.2361
phen-E1	0.2251	0.0900	0.4618	−0.0414	0.3505	0.3825
phen-A	−0.0139	0.0436	0.4103	0.0129	0.3578	0.3280
phen-C3	0.2159	0.1706	0.6008	0.0645	0.4163	0.3751
phen-D	0.2221	0.3092	0.6551	0.0645	0.4157	0.3729
phen-E2	0.2299	0.1311	0.4935	0.0975	0.4499	0.4222
phen-B1	0.1696	0.1258	0.5055	0.1122	0.4660	0.4813
phen-C2	0.1862	0.1171	0.5497	0.1341	0.2203	0.2449
			Carboxylate Structures			
B1	0.0000	0.0000	0.0000	0.0000	0.0000	0.0000
B2	−0.0302	0.0546	0.0566	0.0991	0.0848	0.0424
D2	0.0687	0.1233	0.0955	0.1901	0.1435	0.1043
D1	−0.0096	0.0937	0.0743	0.2245	0.1603	0.0915
B3	−0.0640	0.0915	0.0761	0.2401	0.2196	0.1069
B4	−0.0858	0.1164	0.1019	0.2739	0.2437	0.1126
D3	0.0261	0.1413	0.1310	0.2898	0.2336	0.1469
A	−0.1150	0.3391	0.3685	0.2960	0.2837	0.2282

[a]All energies are given relative to the lowest-energy isomer (carboxylate B1). The structures have been obtained using geometry optimizations with BP86/def2-TZVP and BP86+D3/def2-TZVP (indicated in the second row), and the corresponding single-point energies are provided column-wise for the methods listed in the third row. The isomers are sorted according to their BP86+D3 energy, and all isomers within ∼0.3 eV are included. A full list of all considered isomers is contained in the Supporting Information.

The structures of these conformer families are shown in the Supporting Information. All conformers considered for the phenolate family form a hydrogen bond from the phenolate oxygen to the carboxylic group (hydrogen #7 in Scheme 1, see also Figure 4), leading to a cyclic structure. In addition, the negative charge of the phenolate oxygen is stabilized by a second hydrogen bond with amide hydrogen #6 in conformer families phen-A to phen-F, and also by a third hydrogen bond with the amide hydrogen #5 in conformer families phen-B to phen-F. Finally, for the most stable structural motif phen-C, there is a fourth weak hydrogen bond to the amide hydrogen #4. The structure of phen-C is shown in Figure 4 and the exemplary structures from the other structural families are given in the Supporting Information. Overall, the conformers have very similar backbone conformations, in particular in the vicinity of the self-solvated phenolate group (Figure SI-2 in the Supporting Information).

The lowest-energy carboxylate structures belong to three discernible families A, B, and D. The structural motifs are illustrated in Figure 4, alongside the lowest-energy conformer from each of these families. In the families B and D, the carboxylate oxygen forms ionic H-bonds to the amide hydrogen atoms #3, #5, and #6, with varying relative bond lengths. More specifically, the closest hydrogen bonds involve H#3 (bond lengths of 174−180 pm) and H#5 (200−223 pm) (as highlighted in Figure 4). All B and D structures are characterized by very similar backbone structures. The only difference between these two families is the configuration of the phenol group. For the B structures, the phenol−OH group forms a hydrogen bond to the oxygen of amide group #6, whereas for the D structures a hydrogen bond to the oxygen for amide group #5 is formed. The family A exhibits a different structural motif. Here, one of the oxygen atoms in the carboxyl group is stabilized by a hydrogen bond to the phenol−OH group, whereas the other carboxylic oxygen atoms is involved in a hydrogen bond to the amide hydrogen #4.

Comparing the energies of the conformers calculated with different quantum-chemical methods (Table 2 and Supporting Information), we notice that with BP86 the conformers within one structural family have very similar energies. This order changes, however, when the D3 dispersion correction is included: though already evident in single-point calculations for the BP structures, the effect is even more pronounced after performing the geometry optimizations with BP86+D3. The inclusion of dispersion also changes the relative energy order of the isomers quite significantly. Therefore, we verified the BP86+D3 relative energies with single-point MP2 and SCS-MP2 calculations. Within either the phenolate or the carboxylate structures, the energy order obtained in the BP86+D3 geometry optimizations is mostly preserved between methods.

Comparing the energies of the lowest-energy phenolate and carboxylate structures, the DFT calculations give no conclusive picture. With BP86 (without dispersion corrections), the lowest-energy carboxylate isomer A is ca. 0.1 eV more stable than the lowest-energy phenolate isomer phen-A1. On the other hand, with BP86+D3, the phenolate isomer phen-C1 is approximately 0.1 eV more stable than the lowest-energy carboxylate isomer B1. The picture again changes if the MP2 and SCS-MP2 single-point calculations are considered. In this case, all phenolate isomers are at least 0.2 eV higher in energy than the lowest-energy carboxylate isomer B1. As MP2 and SCS-MP2 should be more reliable than the DFT calculations, we conclude that phenolate structures are energetically unfavorable. Nevertheless, when considering only the relative energies among the phenolate and carboxylate isomers are considered, the BP86+D3 geometry optimizations give relative energies that are consistent with both MP2 and SCS-MP2.

dx.doi.org/10.1021/jp501772d | J. Phys. Chem. A 2014, 118, 8453−8463

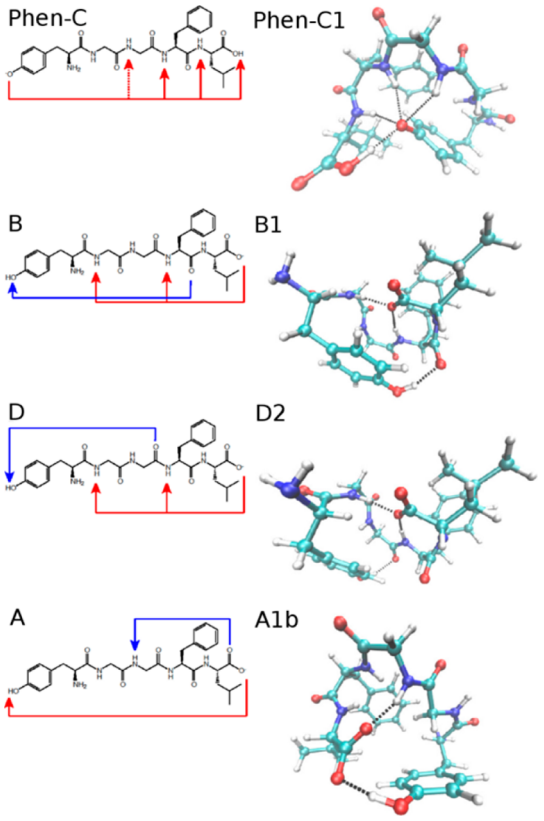

Figure 4. Ground state structures of the energetically most stable conformers of the phen-C family of the phenolate anion and of the A, B, and D structural family for the carboxylate anion. Shown as dashed lines in the structures on the right are the most prominent hydrogen bonds involving the charge carrying group (red arrows in the Lewis structure on the left) and neutral hydrogen bonds (blue arrows in the Lewis structures).

For further interpretation concerning the possible isomeric structures prevailing in experiment, we computed the collision cross sections for all isomers discussed (geometry optimized with DFT/BP86/def2-TZVP) using the projection approximation employing the MOBCAL[61,62] and the SIGMA[63,64] program. The results are depicted in Figure 5 grouped into phenolate and carboxylate isomers. The calculated ccs values are shown as relative deviations $(\Omega^{calc} - \Omega^{exp})/\Omega^{exp}$ from the experimentally determined value of Ω^{exp} = 153.5 Å^2. All structures for which this deviation from experiment is bigger than ±4% can safely be excluded, as this is clearly beyond any experimental and computational error. This eliminates all but the phen-C1 and phen-C2 conformers of the phenolate structures from being significantly present in experiment, whereas within the carboxylate class, only the conformer families A, B, and D are viable candidates (Figure 5).

The candidate carboxylate structures (families A, B, and D) were further refined by generating all conformers accessible by systematically rotating the phenyl and isopropyl side chains. This yields 27 different conformers within each family. These structures were optimized with BP86/def2-TZVP and BP86+D3/def2-TZVP and in addition, single-point energies have been calculated using MP2/def2-TZVP and SCS-MP2/def2-TZVP. The resulting conformer energies are given in Table 3 (for a complete list, see Supporting Information) and these additional conformers are also included in Figure 5. As before, we find that the inclusion of dispersion is essential for

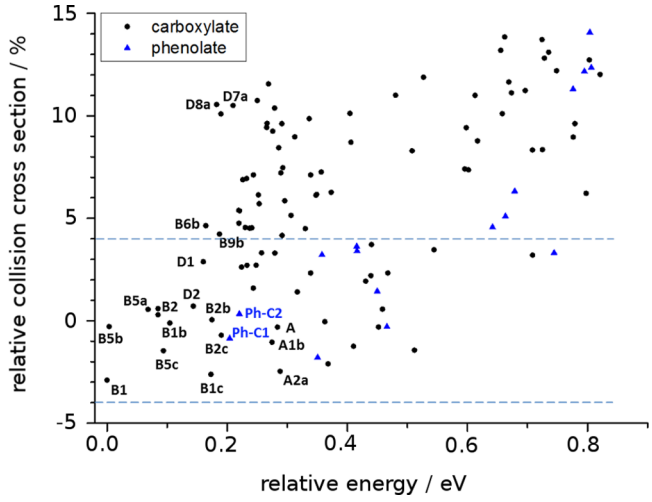

Figure 5. Calculated relative collision cross sections (based on the projection approximation) for DFT/BP86-D3 optimized structures of $[YGGFL - H]^-$, given as deviation from the experimental value of 153.5 Å^2, vs the relative MP2 single-point energy. The zero of energy is taken as the energy of the lowest energy isomer (B1) found for the carboxylate family of structures. The range of ccs considered in this study (±4% of the experimental value) is indicated with dashed lines.

the relative energies, but that the energy order obtained from BP86+D3 geometry optimizations and from MP2 or SCS-MP2 single-point calculations are largely consistent. In particular, the six lowest-energy conformers (all within ca. 0.1 eV) belong to the B family. The most favorable conformer of family D is 0.1–0.2 eV higher in energy than the lowest-energy conformer B1, whereas the most favorable conformer from family A is 0.2–0.3 eV higher in energy.

For most of the low-energy conformers, the ccs is within the experimental limits of 2.7%. However, for the D family we can certainly distinguish between the D1/D2 structures (within ccs limits) and D7a/D8a (outside the ccs limits). On the other hand, family A may be disfavored on energetic grounds, though their collision cross section is within experimental errors. Combining the collision cross sections and the relative energies of all conformers in the A, B, and D families, as shown in Figure 5, we conclude that a structure from the B family is most likely to be present in the experiment. In particular for the low-energy conformers B5b, B5a, B2, and B1b the calculated ccs closely match the measured one.

C. Infrared Photofragmentation Spectra and Comparison with Harmonic Predictions. Figure 6 summarizes the infrared spectra of deprotonated leucine-enkephaline obtained by the IRMPD scheme (taken at room temperature and at 140 K) and by the messenger technique (D2 tagged at 20 K) in the X–H stretch region (X = C, N, O). The IR spectra are taken by monitoring the sum of the b4 and c2 fragment ions (IRMPD, Figure 6a,b) and by the parent anion after D2 loss (messenger technique, Figure 6c). The spectra taken using the IR-MPD scheme show a strong dependence of apparent band intensities as a function of laser fluence (Figure 6a), indicating a strong nonlinearity in molecular photoabsorption behavior. Although a rigorous laser fluence dependence was not attempted in this work, it is obvious that different vibrational bands show different nonlinear behavior in the effective dissociation efficiency of the ion. Empirically, this is based on the observation that some bands do not show up at all at low laser fluences, whereas others begin to saturate and broaden at

dx.doi.org/10.1021/jp501772d | J. Phys. Chem. A 2014, 118, 8453–8463

Table 3. Calculated Energies (eV) and Collision Cross Sections (ccs, Å) of the Most Stable Carboxylate Isomers of Leucine-Enkephaline in the A, B, and D Families[a]

	energy					
	BP86		BP86+D3			
geometry	BP86	BP86+D3	BP86+D3	MP2	SCS-MP2	ccs
B1	0.0000	0.0000	0.0000	0.0000	0.0000	149.1
B5b	−0.0762	−0.0124	0.0367	0.0035	−0.0253	153.1
B5a	−0.0252	0.0381	0.0764	0.0682	0.0362	154.3
B5c	0.0161	0.0523	0.0860	0.0937	0.0700	151.3
B2	−0.0302	0.0566	0.0991	0.0848	0.0424	153.9
B1b	0.0682	0.0822	0.1076	0.1045	0.0820	153.3
B1c	0.1797	0.1767	0.1413	0.1729	0.1722	149.5
D2	0.0687	0.0955	0.1901	0.1435	0.1043	154.6
B2b	0.0574	0.1494	0.1914	0.1746	0.1297	153.6
B2c	0.0961	0.1580	0.1971	0.1901	0.1526	152.4
B6b	−0.1248	0.0465	0.1976	0.1642	0.0532	160.6
D8a	−0.1687	0.0404	0.2241	0.1958	0.0968	169.7
B9b	−0.0394	0.1099	0.2244	0.1870	0.1088	160.0
D1	−0.0096	0.0743	0.2245	0.1603	0.0915	157.9
B6a	−0.0652	0.0958	0.2303	0.2207	0.1113	161.7
D8b	−0.1515	0.0644	0.2312	0.2196	0.1184	169.0
B6c	−0.0232	0.1143	0.2388	0.2301	0.1310	160.5
B3	−0.0640	0.0761	0.2401	0.2196	0.1069	160.8
D7a	−0.1938	0.0398	0.2512	0.2057	0.0721	169.6
B7a	0.0218	0.1482	0.2518	0.2240	0.1527	157.5
D2b	0.1176	0.1867	0.2609	0.2127	0.1568	161.8
B9a	0.0069	0.1592	0.2629	0.2408	0.1619	160.5
D8c	−0.0423	0.1271	0.2677	0.2791	0.1909	164.1
B9c	0.0459	0.1683	0.2710	0.2435	0.1738	155.9
B4	−0.0858	0.1019	0.2739	0.2437	0.1126	164.4
D1a	0.0441	0.1214	0.2740	0.2323	0.1571	164.2
B8a	0.0010	0.1645	0.2769	0.2373	0.1546	160.4
B3b	−0.0303	0.1174	0.2837	0.2533	0.1359	162.3
A1b	−0.1197	0.3368	0.2870	0.2746	0.2185	151.9
A2a	−0.0558	0.3031	0.2896	0.2880	0.2611	149.7
D3	0.0260	0.1310	0.2898	0.2336	0.1469	157.7
D9b	−0.1925	0.0723	0.2918	0.2712	0.1313	170.0
D1c	0.0843	0.1414	0.2936	0.2646	0.1916	162.9
A	−0.1153	0.3683	0.2962	0.2831	0.2271	153.0
B7b	0.0471	0.1901	0.2986	0.2574	0.1809	158.6

[a]All energies are given relative to the lowest-energy isomer (carboxylate B1). The structures have been obtained using geometry optimizations with BP86/def2-TZVP and BP86+D3/def2-TZVP (indicated in the first row), and single-point energies have been calculated with different methods as indicated in the second row. The isomers are sorted according to their BP86+D3 energy, and all isomers within 0.3 eV are included. A full list of all isomers in the A, B, and D families of the carboxylate is contained in the Supporting Information.

high laser fluence. However, given the known challenges (and shortcomings) in IR-MPD methodology the reproducibility between spectra (upper and lower traces in Figure 6a,b, respectively) taken at 300 and 140 K trap temperature is very good. One recognizes a large number of bands, which are well reproduced (in position and width for each spectrum) as well as differences for certain bands.

We first note that, unsurprisingly, there is no observable fundamental signal above 3450 cm^{-1}, which would be indicative of a free O−H stretch, either from a carboxylic group (typically at ∼3570 cm^{-1}) or from the phenol (typically at ∼3640 cm^{-1}). This excludes any isomers bearing a free O−H group (like isomer E, see above), in accordance with the findings based on ion mobility. The strongest feature observed in all experimental configurations used occurs at 2950 cm^{-1} with a shoulder at 2930 cm^{-1} along with weaker bands at 2870, 2985, 3028, and 3063 cm^{-1}. In the region above 3200 cm^{-1}, differences between the two spectroscopic schemes arise: the broad hump between 3200 and 3400 cm^{-1} in the room temperature IRMPD spectrum collapses to a few rather strong bands at 140 K that continue to evolve into two very strong bands at 3270 and 3330 cm^{-1} in the 20 K D_2 predissociation spectrum. Finally, three narrow bands at around 3400 cm^{-1} in the 20K D2 predissociation spectrum (3378, 3392, and 3409 cm^{-1}) are also evident, though broader and blue-shifted (by 5−10 cm^{-1}) from those found in the 140 K and room temperature IRMPD spectra.

Because the candidate isomeric classes differ according to their local intramolecular coupling motifs, we next turned to their vibrational spectra because the resulting band patterns are, in principle, a sensitive probe of the intramolecular contacts in play. Figures 7 and 8 compare the experimental IR spectrum with quantum-chemical predictions for four low-energy members of the B and D family of carboxylate based structures,

dx.doi.org/10.1021/jp501772d | J. Phys. Chem. A 2014, 118, 8453−8463

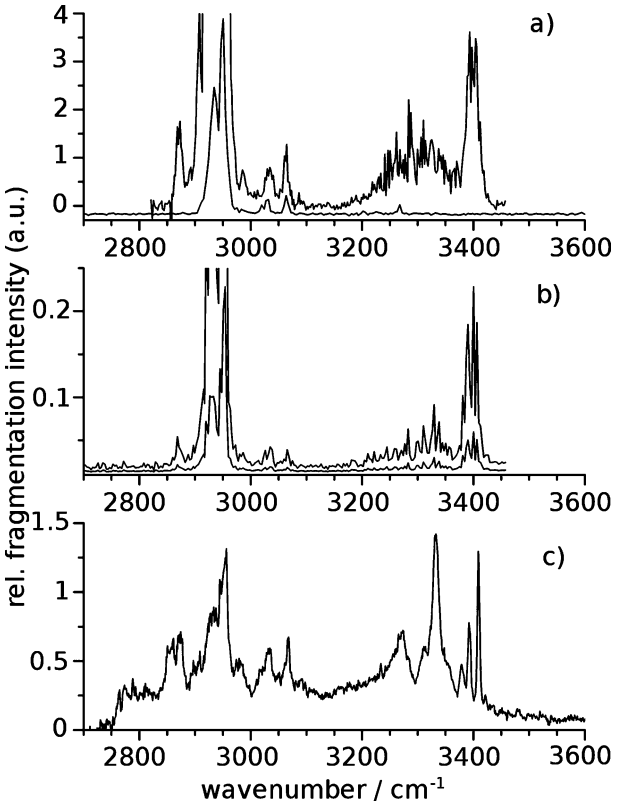

Figure 6. IRMPD spectra of deprotonated leucine-enkephalin taken (a) at room temperature at two different laser fluences (upper trace: ~factor of 5 higher fluence), (b) at T = 140 K (upper trace: scaled by a factor 5), and (c) IR predissociation spectrum of the D_2-tagged anion taken at T = 20 K.

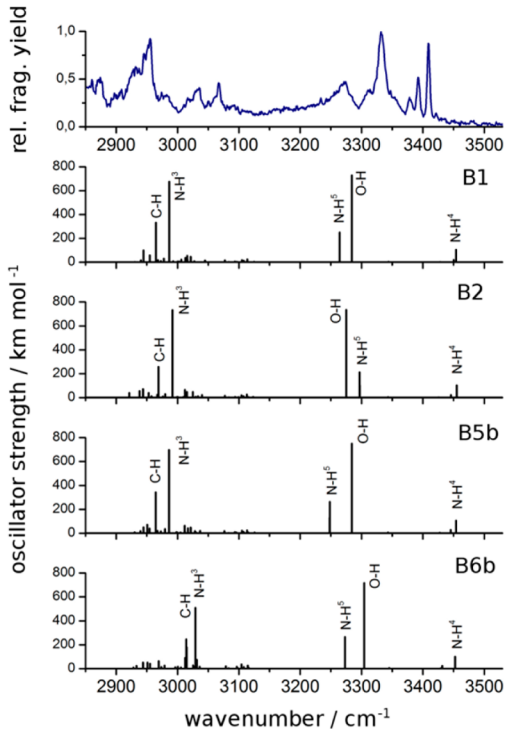

Figure 7. Comparison of computed harmonic vibrational frequencies for B family structures based on a carboxylate anion of [YGGFL − H]$^-$ with experimental 20 K predissociation spectrum (top panel).

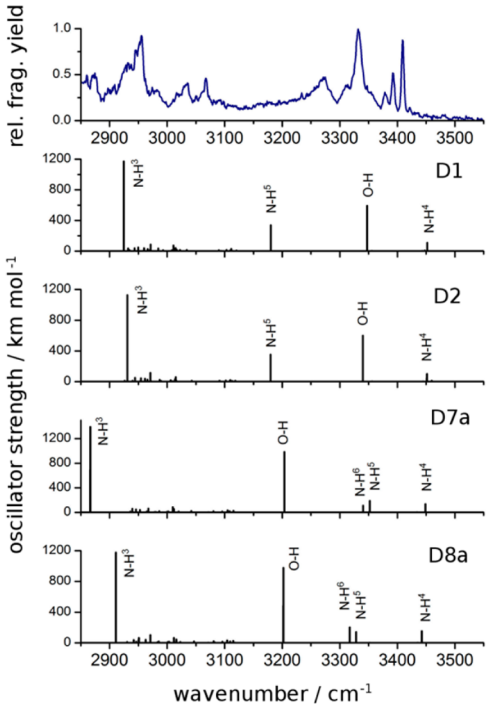

Figure 8. Comparison of computed harmonic vibrational frequencies for D family structures based on a carboxylate anion of [YGGFL − H]$^-$ with experimental 20 K predissociation spectrum (top panel).

respectively. The calculated vibrational spectra of additional low-energy conformers are shown in the Supporting Information. The vibrational modes with highest oscillator strength (labeled on the basis of the numbering of Scheme 1) are indicative of localized N−H or O−H stretch vibrations, which are engaged in a hydrogen bond. As outlined above, the negative charge on the carboxylate group is stabilized to various degrees by H bonds to the peptide NH^x groups (with x = 3, 4, and 5), which in turn enhances the fundamentals of the latter in the IR spectrum.

Within a given family there are substantial shifts in frequency of certain bands; e.g., the N−H^5 band shifts by ~50 cm^{-1} when going from B2 to B5b (Figure 7). On the contrary, other modes like the phenol O−H stretch are rather insensitive to conformational variations (the O−H vibrations stay within ~20 cm^{-1} for all B structures). Within the D family of structures, larger shifts occur for the N−H^3 band. In addition, we note that for the conformers D7a and D8a, the positions of the N−H^5 and O−H bands are exchanged compared to the D1 and D2 conformers. This is related to a change in the orientation of amide group 5 with respect to the backbone in the conformers D7a and D8a. Despite this different assignment, all calculated spectra within the D family are unfortunately rather similar.

What seems to distinguish all members of the B versus the D families are (i) the position of the N−H^5 mode (~3185 ± 6 cm^{-1} for D1/D2 vs 3288 ± 25 cm^{-1} for family B) and (ii) the strength of the C−H stretch mode relative to (and due to a mixing with) the nearby N−H^3 mode predicted only for B conformers. The latter effect can be ascribed to the structure of the B isomers, for which the charge on the carboxylate group comes close to the C−H bond next to the NH_2 group in the tyrosine. This leads to an interaction of the N−H^3 and C−H stretching mode with a small frequency gap between them of

dx.doi.org/10.1021/jp501772d | J. Phys. Chem. A 2014, 118, 8453−8463

~25 cm^{-1}. As a consequence, the C−H stretching mode is drastically increased in intensity leading to the shape of a double peak at around 3000 cm^{-1}.

Comparing this with experiment, one may be inclined to favor B type isomers as the prevailing type of structures in the gas phase on the basis of missing any IR band that could be assigned to the N−H[5] band for D type structures. Second, a "characteristic" partially resolved double feature observed in experiment (at 2930 and 2950 cm^{-1}) is in accordance with predictions for all B type isomers. Thus, the observed vibrational spectra support the assignment obtained on the basis of the ion mobility measurements and the calculated relative energies and would require further site-selective isotope incorporation for confirmation.[65,66] Future work may therefore include the spectroscopic investigation of peptide ions from ^{15}N-labeled amino acids which has been shown to lead to a discernible shift of 6−8 cm^{-1}, e.g., for small molecular anions under IR-MPD conditions.[37]

CONCLUSION

A combination of several mass-spectrometry based experimental techniques in conjunction with ab initio computations have been applied to elucidate the structure of deprotonated leucine-enkephalin anion $[YGGFL - H]^-$. These include determination of the collision-induced dissociation pathways, the absolute collision cross section (using ion mobility), and vibrational spectra. Analysis of these properties with density functional theory indicates that the observed behavior is most consistent with deprotonation at the C-terminus (i.e., to form the carboxylate). The vibrational band pattern suggests that the secondary structure occurs with formation of two types of hydrogen bonds: the negative charge on the C-terminus folds toward the NH group of the peptide bond connecting Y and G, whereas the tyrosine OH group folds toward the C=O group on a peptide bond. The site of the latter interaction likely occurs between either G and F (here called isomer D) or F and L (here called isomer B). Resolution of this ambiguity should be accessible using site-specific isotopic shifts in the vibrational fundamentals. We conclude that the combination of mobility and vibrational spectroscopy, aided by theoretical predictions, will be a powerful tool for the determination of the gas-phase structure adopted by ionic polypeptides, and note that compact structures with charged and neutral intermolecular hydrogen bonds are likely to be common motifs.

ASSOCIATED CONTENT

Supporting Information

Calculated energies of all phenolate and carboxylate isomers of leucine-enkephaline considered, graphical comparison of the structures, comparison of computed harmonic vibrational frequencies for phenolate and carboxylate structures. This material is available free of charge via the Internet at http://pubs.acs.org.

AUTHOR INFORMATION

Corresponding Authors

*C. R. Jacob: e-mail, Christoph.Jacob@kit.edu.
*M. A. Johnson: e-mail, Mark.Johnson@yale.edu.
*M. Kappes: e-mail, Manfred.Kappes@kit.edu.

Notes

The authors declare no competing financial interest.
[#]Deceased April 23, 2014.

ACKNOWLEDGMENTS

This work was partially supported by infrastructure provided by the Helmholtz association through POF "Science and Technology of Nanosystems (STN)". C.R.J. acknowledges funding from the DFG-Center for Functional Nanostructures at KIT. M.A.J. and A.B.W. acknowledge funding from the National Science Foundation under grant CHE-1213634.

REFERENCES

(1) Do, T. D.; LaPointe, N. E.; Economou, N. J.; Buratto, S. K.; Feinstein, S. C.; Shea, J. E.; Bowers, M. T. Effects of pH and Charge State on Peptide Assembly: The YVIFL Model System. *J. Phys. Chem. B* **2013**, *117*, 10759−10768.
(2) Kemper, P. R.; Dupuis, N. F.; Bowers, M. T. A New, Higher Resolution, Ion Mobility Mass Spectrometer. *Int. J. Mass Spectrom.* **2009**, *287*, 46−57.
(3) Dugourd, P.; Hudgins, R. R.; Clemmer, D. E.; Jarrold, M. F. High-Resolution Ion Mobility Measurements. *Rev. Sci. Instrum.* **1997**, *68*, 1122−1129.
(4) Wyttenbach, T.; Bowers, M. T. Gas-Phase Conformations: The Ion Mobility/Ion Chromatography Method. *Top. Curr. Chem.* **2003**, *225*, 207−232.
(5) Vonderach, M.; Ehrler, O. T.; Weis, P.; Kappes, M. M. Combining Ion Mobility Spectrometry, Mass Spectrometry, and Photoelectron Spectroscopy in a High-Transmission Instrument. *Anal. Chem.* **2011**, *83*, 1108−1115.
(6) Giles, K.; Wildgoose, J. L.; Langridge, D. J.; Campuzano, I. A Method for Direct Measurement of Ion Mobilities using a Travelling Wave Ion Guide. *Int. J. Mass Spectrom.* **2010**, *298*, 10−16.
(7) Zucker, S. M.; Ewing, M. A.; Clemmer, D. E. Gridless Overtone Mobility Spectrometry. *Anal. Chem.* **2013**, *85*, 10174−10179.
(8) Bosenberg, W. R.; Guyer, D. R. Broadly Tunable, Single-Frequency Optical Parametric Frequency-Conversion System. *J. Opt. Soc. Am. B* **1993**, *10*, 1716−1722.
(9) Gerhards, M. High Energy and Narrow Bandwidth Mid IR Nanosecond Laser System. *Opt. Commun.* **2004**, *241*, 493−497.
(10) Polfer, N. C.; Oomens, J. Vibrational Spectroscopy of Bare and Solvated Ionic Complexes of Biological Relevance. *Mass Spectrom. Rev.* **2009**, *28*, 468−494.
(11) Lemaire, J.; Boissel, P.; Heninger, M.; Mauclaire, G.; Bellec, G.; Mestdagh, H.; Simon, A.; Caer, S. L.; Ortega, J. M.; Glotin, F.; et al. Gas Phase Infrared Spectroscopy of Selectively Prepared Ions. *Phys. Rev. Lett.* **2002**, *89*, 273002−1−4.
(12) Heine, N.; Fagiani, M. R.; Rossi, M.; Wende, T.; Berden, G.; Blum, V.; Asmis, K. R. Isomer-Selective Detection of Hydrogen-Bond Vibrations in the Protonated Water Hexamer. *J. Am. Chem. Soc.* **2013**, *135*, 8266−8273.
(13) Wolk, A. B.; Leavitt, C. M.; Garand, E.; Johnson, M. A. Cryogenic Ion Chemistry and Spectroscopy. *Acc. Chem. Res.* **2013**, *47*, 202−210.
(14) Gerlich, D. Ion-Neutral Collisions in a 22-Pole Trap at Very-Low Energies. *Phys. Scr.* **1995**, *T59*, 256−263.
(15) Wang, Y. S.; Tsai, C. H.; Lee, Y. T.; Chang, H. C.; Jiang, J. C.; Asvany, O.; Schlemmer, S.; Gerlich, D. Investigations of Protonated and Deprotonated Water Clusters using a Low-Temperature 22-Pole Ion Trap. *J. Phys. Chem. A* **2003**, *107*, 4217−4225.
(16) Rizzo, T. R.; Stearns, J. A.; Boyarkin, O. V. Spectroscopic Studies of Cold, Gas-Phase Biomolecular Ions. *Int. Rev. Phys. Chem.* **2009**, *28*, 481−515.
(17) Kamrath, M. Z.; Relph, R. A.; Johnson, M. A. Vibrational Predissociation Spectrum of the Carbamate Radical Anion, C5H5N-CO_0^-, Generated by Reaction of Pyridine with $(CO_2)_m^-$. *J. Am. Chem. Soc.* **2010**, *132*, 15508−15511.
(18) Goebbert, D. J.; Wende, T.; Bergmann, R.; Meijer, G.; Asmis, K. R. Messenger-Tagging Electrosprayed Ions: Vibrational Spectroscopy of Suberate Dianions. *J. Phys. Chem. A* **2009**, *113*, 5874−5880.
(19) Aebersold, R.; Mann, M. Mass Spectrometry-Based Proteomics. *Nature* **2003**, *422*, 198−207.

(20) Whelan, M.; Kinsella, B.; Furey, A.; Moloney, M.; Cantwell, H.; Lehotay, S. J.; Danaher, M. Determination of Anthelmintic Drug Residues in Milk using Ultra High Performance Liquid Chromatography-Tandem Mass Spectrometry with Rapid Polarity Switching. *J. Chromatogr. A* **2010**, *1217*, 4612−4622.
(21) Waugh, R. J.; Bowie, J. H.; Gross, M. L. Collision-Induced Dissociations of Deprotonated Peptides - Dipeptides Containing ASN, ARG and LYS. *Aust. J. Chem.* **1993**, *46*, 693−702.
(22) Harrison, A. G. Sequence-Specific Fragmentation of Deprotonated Peptides Containing H or Alkyl Side Chains. *J. Am. Soc. Mass Spectrom.* **2001**, *12*, 1−13.
(23) Men, L.; Wang, Y. Fragmentation of the Deprotonated Ions of Peptides Containing Cysteine, Cysteine Sulfinic Acid, Cysteine Sulfonic Acid, Aspartic Acid, and Glutamic Acid. *Rapid Commun. Mass Spectrom.* **2006**, *20*, 777−784.
(24) Pu, D.; Cassady, C. J. Negative Ion Dissociation of Peptides Containing Hydroxyl Side Chains. *Rapid Commun. Mass Spectrom.* **2008**, *22*, 91−100.
(25) Oomens, J.; Steill, J. D.; Redlich, B. Gas-Phase IR Spectroscopy of Deprotonated Amino Acids. *J. Am. Chem. Soc.* **2009**, *131*, 4310−4319.
(26) Woo, H. K.; Lau, K. C.; Wang, X. B.; Wang, L. S. Observation of Cysteine Thiolate and -S···H-O Intermolecular Hydrogen Bond. *J. Phys. Chem. A* **2006**, *110*, 12603−12606.
(27) Tian, Z.; Kass, S. R. Does Electrospray Ionization Produce Gas-Phase or Liquid-Phase Structures? *J. Am. Chem. Soc.* **2008**, *130*, 10842−10843.
(28) Schröder, D.; Buděšínský, M.; Roithová, J. Deprotonation of p-Hydroxybenzoic Acid: Does Electrospray Ionization Sample Solution or Gas-Phase Structures? *J. Am. Chem. Soc.* **2012**, *134*, 15897−15905.
(29) Sztaray, J.; Memboeuf, A.; Drahos, L.; Vekey, K. Leucine Enkephalin-a Mass Spectrometry Standard. *Mass Spectrom. Rev.* **2011**, *30*, 298−320.
(30) Polfer, N. C.; Oomens, J.; Suhai, S.; Paizs, B. Infrared Spectroscopy and Theoretical Studies on Gas-Phase Protonated Leu-Enkephalin and its Fragments: Direct Experimental Evidence for the Mobile Proton. *J. Am. Chem. Soc.* **2007**, *129*, 5887−5897.
(31) Wassermann, T. N.; Boyarkin, O. V.; Paizs, B.; Rizzo, T. R. Conformation-Specific Spectroscopy of Peptide Fragment Ions in a Low-Temperature Ion Trap. *J. Am. Soc. Mass Spectrom.* **2012**, *23*, 1029−1045.
(32) Chen, X. A.; Steill, J. D.; Oomens, J.; Polfer, N. C. Oxazolone Versus Macrocycle Structures for Leu-Enkephalin b(2)-b(4): Insights from Infrared Multiple-Photon Dissociation Spectroscopy and Gas-Phase Hydrogen/Deuterium Exchange. *J. Am. Soc. Mass Spectrom.* **2010**, *21*, 1313−1321.
(33) Vonderach, M.; Ehrler, O. T.; Matheis, K.; Weis, P.; Kappes, M. M. Isomer-Selected Photoelectron Spectroscopy of Isolated DNA Oligonucleotides: Phosphate and Nucleobase Deprotonation at High Negative Charge States. *J. Am. Chem. Soc.* **2012**, *134*, 7830−7841.
(34) Albritton, D. L.; Miller, T. M.; Martin, D. W.; McDaniel, E. W. Mobilities of Mass-Identified H_3^+ and H^+ Ions in Hydrogen. *Phys. Rev.* **1968**, *171*, 94−102.
(35) Kordel, M.; Schooss, D.; Gilb, S.; Blom, M. N.; Hampe, O.; Kappes, M. M. Photodissociation of Trapped Metastable Multiply Charged Anions: A Routine Electronic Spectroscopy of Isolated Large Molecules? *J. Phys. Chem. A* **2004**, *108*, 4830−4837.
(36) Concina, B.; Neumaier, M.; Hampe, O.; Kappes, M. M. Photodetachment of Fullerene Monoanions and Dianions in a Penning Trap: Probes of Delayed Electron Emission and Associated Activation Barriers. *Int. J. Mass Spectrom.* **2006**, *252*, 110−116.
(37) Schinle, F.; Crider, P. E.; Vonderach, M.; Weis, P.; Hampe, O.; Kappes, M. M. Spectroscopic and Theoretical Investigations of Adenosine 5′-Diphosphate and Adenosine 5′-Triphosphate Dianions in the Gas Phase. *Phys. Chem. Chem. Phys.* **2013**, *15*, 6640−6650.
(38) Tang, K. Q.; Tolmachev, A. V.; Nikolaev, E.; Zhang, R.; Belov, M. E.; Udseth, H. R.; Smith, R. D. Independent Control of Ion Transmission in a Jet Disrupter Dual-Channel Ion Funnel Electrospray Ionization MS Interface. *Anal. Chem.* **2002**, *74*, 5431−5437.
(39) Wilcox, B. E.; Hendrickson, C. L.; Marshall, A. G. Improved Ion Extraction from a Linear Octopole Ion Trap: SIMION Analysis and Experimental Demonstration. *J. Am. Soc. Mass Spectrom.* **2002**, *13*, 1304−1312.
(40) Hampe, O.; Karpuschkin, T.; Vonderach, M.; Weis, P.; Yu, Y. M.; Gan, L. B.; Klopper, W.; Kappes, M. M. Heating a Bowl of Single-Molecule-Soup: Structure and Desorption Energetics of Water-Encapsulated Open-Cage [60] Fullerenoid Anions in the Gas-Phase. *Phys. Chem. Chem. Phys.* **2011**, *13*, 9818−9823.
(41) Karpuschkin, T.; Kappes, M. M.; Hampe, O. Binding of O_2 and CO to Metal Porphyrin Anions in the Gas Phase. *Angew. Chem., Int. Ed. Engl.* **2013**, *52*, 10374−10377.
(42) Kamrath, M. Z.; Relph, R. A.; Guasco, T. L.; Leavitt, C. M.; Johnson, M. A. Vibrational Predissociation Spectroscopy of the H_2-Tagged Mono- and Dicarboxylate Anions of Dodecanedioic Acid. *Int. J. Mass Spectrom.* **2011**, *300*, 91−98.
(43) Case, D. A.; Pearlman, D. A.; Caldwell, J. W.; Chearham, T. E., III; Wang, J.; Ross, W. S.;Simmerling, C. L.; Darden, T. A.; Merz, K. M.; Stanton, R. V.; et al.. *AMBER7* (2002), University of California, San Francisco.
(44) MOPAC 2009; Stewart, J. J. P. *MOPAC 2009*; Stewart Computational Chemistry: Colorado Springs, CO, 2008.
(45) Ahlrichs, R.; Bär, M.; Häser, M.; Horn, H.; Kölmel, C. Electronic Structure Calculations on Workstation Computers: the Program System TURBOMOLE. *Chem. Phys. Lett.* **1989**, *162*, 165−169.
(46) Becke, A. D. Density-Functional Exchange-Energy Approximation with Correct Asymptotic Behavior. *Phys. Rev. A* **1988**, *38*, 3098−3100.
(47) Perdew, J. P. Density-Functional Approximation for the Correlation Energy of the Inhomogeneous Electron Gas. *Phys. Rev. B* **1986**, *33*, 8822−8824.
(48) Weigend, F.; Häser, M.; Patzelt, H.; Ahlrichs, R. RI-MP2: Optimized Auxiliary Basis Sets and Demonstration of Efficiency. *Chem. Phys. Lett.* **1998**, *294*, 143−152.
(49) Grimme, S. Accurate Description of van der Waals Complexes by Density Functional Theory Including Empirical Corrections. *J. Comput. Chem.* **2004**, *25*, 1463−1473.
(50) Grimme, S. Semiempirical GGA-type Density Functional Constructed with a Long-Range Dispersion Correction. *J. Comput. Chem.* **2006**, *27*, 1787−1799.
(51) Grimme, S. Improved Second-Order Møller−Plesset Perturbation Theory by Separate Scaling of Parallel- and Antiparallel-Spin Pair Correlation Energies. *J. Chem. Phys.* **2003**, *118*, 9095−9102.
(52) Neugebauer, J.; Reiher, M.; Kind, C.; Hess, B. A. Quantum Chemical Calculation of Vibrational Spectra of Large Molecules–Raman and IR Spectra for Buckminsterfullerene. *J. Comput. Chem.* **2002**, *23*, 895−910.
(53) Weymuth, T.; Haag, M. P.; Kiewisch, K.; Luber, S.; Schenk, S.; Jacob, C. R.; Herrmann, C.; Neugebauer, J.; Reiher, M. M(O)V(I)-P(AC): Vibrational Spectroscopy with a Robust Meta-Program for Massively Parallel Standard and Inverse Calculations. *J. Comput. Chem.* **2012**, *33*, 2186−98.
(54) Laury, M. L.; Boesch, S. E.; Haken, I.; Sinha, P.; Wheeler, R. A.; Wilson, A. K. Harmonic Vibrational Frequencies: Scale Factors for Pure, Hybrid, Hybrid Meta, and Double-Hybrid Functionals in Conjunction with Correlation Consistent Basis Sets. *J. Comput. Chem.* **2011**, *32*, 2339−2347.
(55) Roepstorff, P.; Fohlman, J. Letter to the Editors. *Biol. Mass Spectrom.* **1984**, *11*, 601−601.
(56) Biemann, K. Contributions of Mass-Spectrometry to Peptide and Protein Structure. *Biomed. Environ. Mass Spectrom.* **1988**, *16*, 99−111.
(57) Harrison, A. G.; Young, A. B. Fragmentation of Deprotonated N-Benzoylpeptides: Formation of Deprotonated Oxazolones. *J. Am. Soc. Mass Spectrom.* **2004**, *15*, 446−456.
(58) Harrison, A. G.; Siu, K. W. M.; El Aribi, H. Amide Bond Cleavage in Deprotonated Tripeptides: a Newly Discovered Pathway to " b(2) Ions. *Rapid Commun. Mass Spectrom.* **2003**, *17*, 869−875.

(59) Polfer, N. C.; Bohrer, B. C.; Plasencia, M. D.; Paizs, B.; Clemmer, D. E. On the Dynamics of Fragment Isomerization in Collision-Induced Dissociation of Peptides. *J. Phys. Chem. A* **2008**, *112*, 1286−1293.
(60) Soper, M. T.; DeToma, A. S.; Hyung, S. J.; Lim, M. H.; Ruotolo, B. T. Amyloid-Beta-Neuropeptide Interactions Assessed by Ion Mobility-Mass Spectrometry. *Phys. Chem. Chem. Phys.* **2013**, *15*, 8952−8961.
(61) Mesleh, M. F.; Hunter, J. M.; Shvartsburg, A. A.; Schatz, G. C.; Jarrold, M. F. Structural Information From Ion Mobility Measurements: Effects of the Long-Range Potential. *J. Phys. Chem.* **1996**, *100*, 16082−16086.
(62) Shvartsburg, A. A.; Jarrold, M. F. An Exact Hard-Spheres Scattering Model for the Mobilities of Polyatomic Ions. *Chem. Phys. Lett.* **1996**, *261*, 86−91.
(63) Wyttenbach, T.; vonHelden, G.; Batka, J. J.; Carlat, D.; Bowers, M. T. Effect of the Long-Range Potential on Ion Mobility Measurements. *J. Am. Soc. Mass Spectrom.* **1997**, *8*, 275−282.
(64) Wyttenbach, T.; Witt, M.; Bowers, M. T. On the Stability of Amino Acid Zwitterions in the Gas Phase: The Influence of Derivatization, Proton Affinity, and Alkali Ion Addition. *J. Am. Chem. Soc.* **2000**, *122*, 3458−3464.
(65) Stearns, J. A.; Seaiby, C.; Boyarkin, O. V.; Rizzo, T. R. Spectroscopy and Conformational Preferences of Gas-Phase Helices. *Phys. Chem. Chem. Phys.* **2009**, *11*, 125−132.
(66) Garand, E.; Kamrath, M. Z.; Jordan, P. A.; Wolk, A. B.; Leavitt, C. M.; McCoy, A. B.; Miller, S. J.; Johnson, M. A. Determination of Noncovalent Docking by Infrared Spectroscopy of Cold Gas-phase Complexes. *Science* **2012**, *335*, 694−698.